Sensors and Materials, Vol. 38, No. 4 (2026) 1803–1815
MYU Tokyo

S & M 4407

Design, Fabrication, and Characterization of a Textile Force-sensitive Resistor as a Building Block towards Smart Socks

Filip Mrkić,[1*] Lazar Milić,[1] Bojan Petrović,[2] Igor Putnik,[1] Saima Qureshi,[1] Sanja Kojić,[1] Pedro Galdames,[3] Guillaume Sérandour,[3] and Goran M. Stojanović[1]

[1]Faculty of Technical Sciences, University of Novi Sad, Trg Dositeja Obradovića 6, Novi Sad 21000, Serbia
[2]Faculty of Medicine, University of Novi Sad, Hajduk Veljkova 3, Novi Sad 21000, Serbia
[3]Faculty of Engineering, Universidad Austral de Chile, Calle General Lagos 2086, Valdivia 5090000, Chile

(Received December 29, 2025; accepted March 9, 2026)

Keywords: gait assessment, wearable devices, wearable sensors

With the dawn of wearable electronics, textile has become a natural avenue for incorporating devices with the goal of easing everyday life. Wearable electronics has found its use in medicine by enforcing concepts such as telemedicine and passive data acquisition. Now, textile electronics has begun to show its high potential in the healthcare field, through noninvasive devices or assistive parts to conventional electronic equipment. In gait analysis, the use of commercial force-sensing resistors (FSRs) has shown high applicability; however, their coarseness in contact with the skin has yet to be overcome. In this paper, we present the design, fabrication, and characterization of FSRs, completely based on conductive textiles and thread, with a polyvinyl chloride (PVC) spacer foil. Two shapes of the interdigitated electrodes were explored, aside from varying the number of gaps in the PVC spacer (which defines the total contact area), to find the optimal combination that would best suit the transducer in terms of sensitivity. The sensitivity, repeatability, and reproducibility of each of the possible shape and contact area combinations were calculated. Finally, the feasibility of a textile-based FSR sock for gait analysis is presented. The showcased FSRs demonstrate that there is a high potential for the application of the proposed FSRs in wearable devices, not only for gait analysis, but also in physical rehabilitation procedures.

1. Introduction

Gait analysis plays a significant role in many domains of medicine, such as health monitoring, physical rehabilitation, sports science, as well as elderly care, as it offers crucial insights in locomotion patterns and musculoskeletal system functioning. Globally, 2.41 billion people are afflicted with conditions that could benefit from physical rehabilitation.[1,2] Out of that, 1.71 billion people have musculoskeletal disorders, which is a 63% increase from 1999 to 2019.[1]

*Corresponding author: e-mail: filip.mrkic@uns.ac.rs
https://doi.org/10.18494/SAM6145

ISSN 0914-4935
https://myukk.org/

Gait monitoring and quantification opens new horizons into diagnosing neuromuscular disorders,[3,4] evaluating recovery progress[5] and optimizing athletic performance.[6] An estimated number of 684000 fatal falls occur every year, and 37.3 million falls are severe enough to require medical attention.[7] With that in mind, accurate gait metrics are especially important for elderly care, as they provide an early detection of mobility issues.[8] Conventionally, gait analysis and quantification rely on laboratory-based systems, such as force plates, motion capture systems,[6,9] and specially modified treadmills.[10,11] Even though these setups are highly accurate and precise, they are commonly expensive and require a controlled environment, aside from medical staff being present. Additionally, they limit patient movement to confined spaces and a certain time period.[12] Therefore, these setups are not only inaccessible to many clinicians and daily-life evaluations, but also lack natural validity, as they are confined to artificial testing conditions.[12,13]

Analyses of plantar pressure distribution during gait highlight key sensor placement regions where pressure changes are most prominent. At the heel, medial and lateral zones experience peak loads during heel strike and terminal stance, with lateral shifts during propulsion, while the central heel remains more stable.[14–18] In the forefoot, the 1st metatarsal head is critical at foot flat and toe-off, showing pressure increases of up to 57.8% in normal gait, while the 5th metatarsal head contributes during terminal stance and push-off.[14,16,18,19] The hallux peaks in pre-swing, with pressures dropping by as much as 63.2% in altered gait patterns.[20,21] Functionally, gait phases correspond to posterior/lateral heel loading (heel strike), 1st metatarsal (foot flat), and hallux/5th metatarsal (toe-off).[14–19] These regions combine high peak forces with dynamic transitions, making them optimal for sensor placement, particularly the medial/lateral heel and 1st and 5th metatarsals.[15–17] Textile-integrated force-sensing resistors (FSRs), owing to their thinness, flexibility, and robustness, can capture these localized changes without compromising comfort. Unlike costly lab-based systems, embroidered FSR socks or insoles allow portable, real-time gait monitoring in natural settings, supporting rehabilitation, musculoskeletal assessment, and neuromotor recovery. Their resolution and durability make them especially suitable for elderly users, stroke survivors, and individuals with neuromuscular conditions.[14–19]

With the development of electronics, through miniaturization and novel fabrication techniques and materials, there has been an ever-growing expansion in wearable technologies.[22–24] Through wearables, users are capable of passively obtaining large amounts of data pertaining to their gait, which are stored and/or sent to their healthcare provider for analysis.[25] This enables long-term monitoring in real-world settings, aside from reflecting natural movement patterns outside of clinical laboratories.[26] Moreover, these wearable systems offer a cost-effective, portable, and unnoticeable alternative, promoting continuous data acquisition during everyday activities.[27] They improve the accessibility and scalability of gait-related diagnostics.[28]

Recently, over the past years, there has been a shift towards wearable solutions through the integration of sensors directly into textiles, with the goal of creating unobtrusive, comfortable, and user-friendly systems.[27] These textile-based systems incorporate not only textile transducers[29] in everyday clothing, but also 3D-printed flexible structures,[30] optical fibers,[31]

conductive polymers,[32] and even microfluidic devices,[33] all with the goal of harnessing as much data to provide accurate and reliable results.

Textile-based transducers, incorporated into sensing systems, particularly those embedded in garments such as socks or insoles, provide localized pressure measurements associated with gait phases.[34,35] This makes them ideal for on-body gait assessment. Such innovations align significantly with the increasing demand for smart clothing capable of blending seamlessly into users' wardrobes. However, there is still a long way for widespread use to be achieved. Some of the most demanding obstacles are sensor durability, measurement accuracy, and reliable interfacing with electronics for signal acquisition, transmission, and analysis. One key point is the need for the standardization of connections between conventional pin-hole and textile electronics, which is a current topic in recent years.[36]

In comparison with capacitive transducers, resistive transducers have been more frequently integrated in insoles and socks. These transducers can be made of, as previously stated, conductive polymers and functionalized thread;[37] however, the integration of FSRs into everyday garments using embroidery techniques has gained scientific popularity.[38,39] It presents a promising solution, combining material flexibility with reproducible fabrication processes. Hoseini *et al.* developed a system with an FSR transducer for gait phase detection employing machine learning. They achieved a clear detection of the standing and swing phases, which comprised 2/3 and 1/3, respectively, on average.[40] Additionally, Heng *et al.* developed a similar system for gait phase differentiation, incorporating single-walled and multi-walled carbon nanotubes (SWCNT and MWCNT, respectively) in their FSRs, to increase sensitivity and reliability.[41] Moreover, they extracted accurately the angle information at which the leg is positioned. Pant *et al.* extracted the gait phase from FSRs positioned at various locations in the insole and successfully trained classifiers (support vector machine, naïve Bayes, and decision tree) to categorize and identify different gait phases.[42] In this paper, we present a completely embroidered and customized FSR, which has been fully characterized in terms of reproducibility, repeatability, sensitivity, output range, hysteresis, response, and relaxation time. Furthermore, we have integrated FSRs into a sock. The sock contains four FSRs specifically placed to analyze the weight distribution aside from gait analysis. The sensors on the sock were tested in a laboratory setting.

2. Data, Materials, and Methods

2.1 Sensor design and fabrication

The textile-based FSR was designed in AutoCAD 2024 (Autodesk, California, USA). The interdigitated electrodes were fabricated on the ZSK JCZA 0109-550 embroidery machine (ZSK, Germany), whilst the spacer was fabricated from polyvinyl chloride (PVC) foil, with a thickness of 100 μm, on the GRAPHTEC CE6000-60 cutting plotter (GRAPHTEC, Japan). The conductive fabric used as the active sensing layer was Shieldex® Tulle (Statex Produktions- und Vertriebs GmbH, Germany), a commercially available silver-plated polyamide textile. Silver thread was used for the embroidery process (SilverTex100, Statex Produktions- und Vertriebs

GmbH, Germany). This fabric was selected owing to its high electrical conductivity (surface resistivity < 0.02 Ω/sq), mechanical flexibility, and proven stability under repeated mechanical deformation. Compared with alternative conductive fabrics, Shieldex® Tulle offers a balance between sensitivity, washability, and availability in large sheets, which makes it particularly suitable for reproducible sensor fabrication. Its porous structure also facilitates intimate contact with the embroidered electrodes, ensuring consistent pressure-to-resistance transduction. Other commercially available conductive textiles were considered, but Shieldex® Tulle was chosen as it provided the most stable baseline resistance and repeatable response during preliminary characterization. Two sensor designs were created. The first sensor design is square, whereas the second one is circular. The working areas of both sensors were the same, approximately 900 mm^2. The holes in all sensor designs were square and had an area of 4 mm^2. In total, four different designs were fabricated, varying the shape design (square and circular) and the spacer perforation (11 and 16%). A sample FSR structure is shown in Fig. 1.

The aforementioned spacer was cut into 5 × 5 and 6 × 6 matrices. Taking this into consideration, the percentages of the cut-out areas were 11 and 16%, respectively. The circular spacers were designed to have the same hole area by adjusting the distance between the holes. The relations used to achieve the same hole area are shown in Eqs. (1) and (2), where S_{foil} is the surface of the foil (30 × 30 mm^2), S_{space} is the surface of one cutout square space (2 × 2 mm^2), m is the number of columns and rows of squares that are cut out of the foil, and x is the scaling factor that corresponds to the amount of noncut space [Eq. (1)], which shows a parametric relation between the surface of the foil, S_{foil}, on one side and the number of rows and columns, m, and the scaling factor x on the other side. By varying x, where $x \in (0,1)$, m can be determined for it to be a natural number ($m \in N$).

$$S_{foil} = S_{space} \cdot m^2 + S_{foil} \cdot x \tag{1}$$

$$m^2 = \frac{S_{foil}}{S_{space}}(1-x) \tag{2}$$

The thread used for electrode embroidery was 120 Tex 28 (Silvertech, Indiana, USA). This thread showed the lowest resistance per unit length out of all available Silvertech threads. The embroidered design also followed both square and circular designs. The number of fingers between the two designs was kept the same. For the conductive top layer, a commercial copper-based conducting fabric, Shieldex Kiel SK 96 (Shieldex, Germany), was used. The assembly process and the final design are shown in Fig. 2.

2.2 Sensor characterization

For sensor characterization, a 34SC-2 tension testing platform (Instron, Massachusetts, USA) was used, alongside an LCZ (inductance-capacitance-impedance) meter (U1733C, State of California, USA, Keysight). Controlled compressive tests were performed on the tension testing

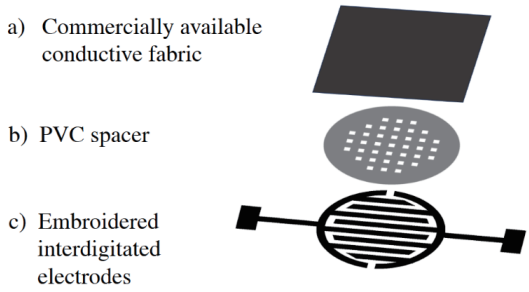

Fig. 1. Exploded view of one of the FSR designs used.

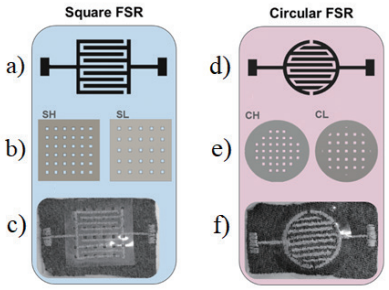

Fig. 2. (Color online) Graphic depiction of the assembly process and the final design of the textile-based FSR: (a) square IDE, (b) spacer filled with 5 × 5 and 6 × 6 cutouts, (c) finished sample without the top conductive fabric, (d) circle IDE, (e) spacer with 11 and 16% cut out of it, and (f) finished sample without the top conductive fabric.

platform, while the change in resistance was measured on the LCZ meter. The applied force ranged from 0 to 200 N. Readings of measurement of the LCZ meter were taken in increments of 5 N, adding to 40 measuring points per measurement. The sensors were characterized in terms of sensitivity, repeatability, reproducibility, hysteresis, and response time. A calibration curve was determined, as well as the output and input ranges.

To explore the sensitivity of a nonlinear sensor, three different pathways were taken. The sensor's resistive response was modeled using exponential [Eqs. (3)–(6)] and logarithmic [Eqs. (7)–(9)] functions of force. The sensitivities of these functions were calculated, as well as the differential approximation of the exponential one. The data were fitted using an exponential function, as shown in Eq. (3), which was normalized with the resistance at which the maximum force is applied and with the maximum force itself. This can be seen in Eq. (4), where a and b from Eq. (3) are fitted parameters, and c is calculated from Eq. (4). The normalized force and resistance are denoted with f and r, respectively, as shown in Eq. (5), whereas the final normalized exponential relation between force and resistance is shown in Eq. (6).

$$R(F) = b \cdot F^{-a} \tag{3}$$

$$R(F)/R_{Fmax} = c \cdot \left(F/F_{max}\right)^{-a}; \; c = b \cdot F_{max}^{-a}/R_{Fmax} \tag{4}$$

$$r_{exp} = R(F)/R_{Fmax}; \; f = F/F_{max} \tag{5}$$

$$r_{exp}(f) = c \cdot f^{-a} \tag{6}$$

Furthermore, a logarithmic function was used as well, with the goal of obtaining a logarithmic sensitivity, which is not dependent on the measurement value, but a constant approximation. The logarithmic fit can be seen in Eq. (7), where d denotes the fit constant, obtained from c and a. The logarithmic force is denoted as n, as seen in Eq. (8), whereas Eq. (9) shows the end result of the previously presented substitution.

$$r_{log}(f) = d \cdot \log_{10}(f) \tag{7}$$

$$n = \log_{10}(f) \tag{8}$$

$$r_{log}(n) = d \cdot n \tag{9}$$

Sensitivity equations are shown as Eqs. (10)–(14). Equations (10) and (11) represent the derivative equations of the exponential fit in Eq. (6), denoted with S_{exp}. Additionally, the derivative of the logarithmic fit [Eq. (9)] is shown in Eqs. (12) and (13) and denoted with S_{log}. Finally, the approximate sensitivity, denoted with S, is shown in Eq. (14). In Eq. (14), Δr is the output range, Δf is the input range, and $r(f_{max})$ and $r(f_{min})$ are the normalized resistances for the maximum force f_{max} and minimum force f_{min}, respectively. The presented sensitivities give accurate values of change per point; however, to obtain a more general value, linear and part-by-part linear sensitivity will be used in the following analysis:

$$S_{exp} = \frac{dr_{exp}(f)}{df} = \frac{d}{df}\left(c \cdot f^{-a}\right), \tag{10}$$

$$S_{exp} = d \cdot f^{-a-1}; d = -c \cdot a, \tag{11}$$

$$S_{log} = \frac{dr_{log}(f)}{dn} = \frac{d}{dn}(d \cdot n), \tag{12}$$

$$S_{log} = d, \tag{13}$$

$$S \approx \left|\frac{\Delta r}{\Delta f}\right| = \left|\frac{r(f_{max}) - r(f_{min})}{f_{max} - f_{min}}\right|. \tag{14}$$

After the analysis of sensitivity, reproducibility, repeatability, hysteresis, and input and output ranges were calculated, as well as response time and settling force. Response time was approximated through sampling frequency. Hysteresis was measured for the sensor with the highest reproducibility, as four of those will be implemented in the gait measurement system.

The hysteresis error was calculated as shown in Eq. (15), where $r_{up}(f)$ is the normalized resistance when force is increasing, $r_{down}(f)$ is the normalized resistance when force is decreasing, and Δ_{output} is the full-scale output span of the sensor.

$$H(\%) = \frac{\max\left|r_{up}(f) - r_{down}(f)\right|}{\Delta_{output}} \cdot 100 \tag{15}$$

Following sensor characterization, the sensors were sewn onto a sock. Lines made from silver thread were sewn from each FSR, connecting them to the developed readout electronics.

3. Results

3.1 Sensor design selection

For each of the four different designs, three samples were fabricated. Five measurements were performed per sample, applying force from 0 to 200 N. Each design was denoted differently with either S – square or C – circle, coming from the design of the IDE shape, and H – high or L – low, coming from the amount of cut space (e.g., *SH* stands for "square high", meaning that the FSR is square and has more cutout space in the spacer foil). The repeatability and reproducibility of the sensors were calculated, alongside sensitivity. For the sensor design with the highest sensitivity, further characterization was performed in terms of hysteresis, response time, relaxation time, and settling force. This design was also fabricated and embroidered on the finalized sock. As shown in Table 1, the design of the square FSR with a spacer cutout factor of 16% (*SH*) showed the highest repeatability (lowest percentage repeatability error), and it has the lowest reproducibility error as well. Its output range is lower than that of the design with a spacer cutout factor of 11% (*CL*). The reproducibility error of 8.08% and the repeatability error of 1.73% show high potential in the applicability of this fabrication method in producing reliable FSR transducers. However, sensitivity and output range must be considered, as they define how well the transducer can detect minimal changes in its respective application.

Figure 3 shows the transfer curve of each FSR design. It shows high overlap; however, the *CH* FSR has a lower resistance in the steady state. Three distinct regions can be defined using the closeness of the rate of change, 0–10, 10–50, and 50–200 N, in which the transfer curve behaves increasingly slower. The data were fit using Eq. (6), which when transformed using a logarithmic scale was Eq. (9). To determine the quality of fit of all four models, R^2 was used as the quantifying metric. The design with the highest R^2 score of 98.6% was the *CL* design, followed by *SL* (97.9%), *CH* (95.9%), and finally, *SH* (87.2%). This shows that the *CL* design had the highest fit; more precisely, it explains the variance of the system the best, among all the designs.

Sensitivity is presented in two ways: linear sensitivity, which represents the ratio between the input and output ranges, and part-to-part sensitivity, where the measurement space was divided into three groups (0–10, 10–50, and 50–200 N), based on the rate of change or the first derivative of the transfer function. Where the rate of change was in the margin of error, those ranges were

Table 1
Calculated sensor characteristics (S – square; C – circular; L – low amount of cut space; H – high amount cut space).

Design type	Repeatability (%)	Reproducibility (%)	Output range (Ω)
SL	1.97	6.80	96.85
SH	1.73	8.08	76.09
CL	3.40	20.78	140.16
CH	2.13	11.87	114.63

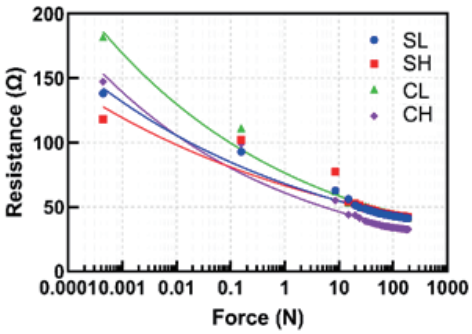

Fig. 3. (Color online) Transfer curves [R(F)] for all four proposed FSR designs.

grouped. These two resulting sensitivities can be seen in Tables 2 and 3. What can be seen by comparing these two tables is that in terms of the first approximation, linear sensitivity shows the highest change for the circular design with a cutout factor of 11% (*CL*). However, the main contribution to the rate of change is in the first region (0–10 N), for this sensor design, as shown in Table 3. In the other regions, the transducers change closely like the other three designed transducers. This leads to options such as fitting. Furthermore, logarithmic sensitivity was analyzed, as shown in Table 2. This was carried out using Eq. (9). Although the *CL* sensor has the lowest reproducibility and repeatability from the four designs, these are parameters that can be adjusted by standardizing the fabrication process better and by pre-calibrating the measurements. This sensor shows the highest R^2 score and linear and logarithmic sensitivities, as well as good part-to-part linear sensitivity.

3.2 Final sensor characterization

For further characterization and integration in smart socks, the *CL* design was used, as it has the highest sensitivity and output range. Reproducibility and repeatability can be compensated through calibration curves. Its hysteresis, response time, settling force, and relaxation time were calculated. Moreover, the calibration curve was tested for accuracy.

Figure 4 shows hysteresis results with the hysteresis error calculated from Eq. (13) being 6.11%. The aforementioned figure shows a high overlap between the compressive and decompressive curves; however, notably in every measurement cycle, the decompressive curve was lower than the compressive one.

The calibration curve shown in Fig. 5 has an R^2 score of 99.89%. The plotted graph in Fig. 5 shows the same plot as *CH* from Fig. 3, obtained using the leave-one-out cross-validation

Table 2
Linear and logarithmic sensitivities.

Design type	Linear sensitivity (Ω/N)	Logarithmic sensitivity
SL	0.48	6.49
SH	0.38	5.61
CL	0.71	8.80
CH	0.58	7.29

Table 3
Part-to-part linear sensitivity.

Range (N)	*SL* (Ω/N)	*SH* (Ω/N)	*CL* (Ω/N)	*CH* (Ω/N)
0–10	7.54	4.09	11.94	9.21
10–50	0.26	0.19	0.14	0.19
50–200	0.02	0.02	0.03	0.03

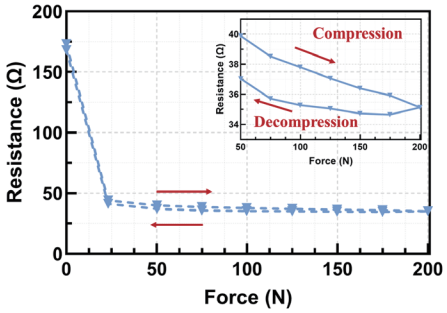

Fig. 4. (Color online) Hysteresis results.

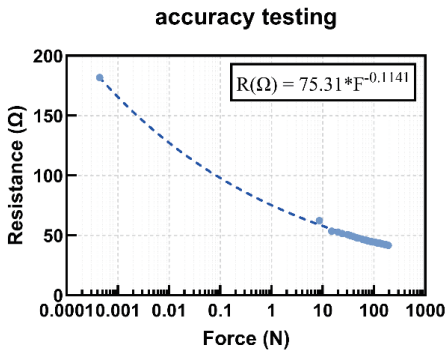

Fig. 5. (Color online) Calibration curve.

method. The curve was fit for the compression part of the hysteresis. To test the accuracy and the deviation of the fit curve from the measured data, five points from five different force ranges were taken and their corresponding values were calculated, as shown in Table 4.

The highest absolute error and lowest accuracy are for lower forces, where the resistance is higher. However, the absolute and accuracy errors decrease considerably on higher forces. The mean absolute error (*MAE*) was calculated as 3.89, whereas the root mean square error (*RMSE*) as 8.13. When analyzing over the full sensor scale (%*FS*), *MAE* (%*FS*) is 2.78% and *RMSE* (%*FS*) is 5.81%, which shows a highly adequate calibration curve to the data.

Finally, settling force was measured as the force at which the resistance becomes 95% of its steady state value (111 N). The time needed for the sensor to decompress and return to its initial high resistance is 2.7 s, whereas the rising time depends on the initial displacement rate of the testing method. In the proposed application, the applied force or displacement rate is initially high, as it is related to the weight of the body. The response time was not directly measured but estimated from the acquisition resolution of 20 ms. Since no transient behavior was observable between consecutive samples, the response time is inferred to be shorter than the temporal resolution of the measurement system. Therefore, only an upper bound of approximately 20 ms can be established.

Table 4
Calibration curve testing.

Measured R (Ω)	Calculated R (Ω)	Error (Ω)	Relative error	Accuracy error (%)
111.234	93.054	18.18	0.163	12.9711
47.142	47.662	0.52	0.011	0.371
44.429	44.529	0.1	0.002	0.071
42.741	42.361	0.38	0.008	0.271
41.808	41.514	0.294	0.007	0.209

4. Discussion

The observed exponential resistance–force response, with a rapid change below 10 N and a slower variation at higher loads, motivated our use of a logarithmic model. This choice allowed the direct comparison of different sensor geometries and spacer perforations without circuit conditioning. While amplifier-based approaches (e.g., FlexiForce A201 inverting configuration) can linearize conductance versus force, our focus here was on intrinsic sensor behavior. For the intended FSR sock application, the steep low-force response is advantageous for detecting contact events (heel strike and toe-off), whereas precise linearization will be addressed in the next stage through voltage-divider or amplifier circuits.

The calibration curve exhibited an expected trend of high nonlinearity, which is present in FSR sensors.[20,43,44] In terms of sensitivity, the sensor with a spacer cutout factor of 89% (*CL*) demonstrated consistent overall linear sensitivity across the range of 0–200 N. When analyzing specific sections of the input range (0–200 N), the highest sensitivity was observed in the lower force range (0–10 N). The hysteresis, response time, and settling force measurements also showed favorable performance, with minimal discrepancies between loading and unloading cycles (approximately 6%), and short response times (< 20 ms) that are crucial for real-time gait monitoring. Overall, the sensor design demonstrated good potential for wearable gait analysis, especially in terms of its performance, cost-effectiveness, and ease of integration into textile-based systems. Recent studies have explored textile-based force and strain sensors for wearable applications. Tangsirinaruenart and Stylios developed stitch-based strain sensors, revealing that a 304 two-ply stitch structure offered the highest performance with good linearity, a low hysteresis of 6.25%, and high repeatability.[45] Liang *et al.* compared various conductive fabrics for stretch sensors, noting that silver-plated yarn sensors exhibited superior sensitivity and linearity.[46] Goy *et al.* fabricated wearable pressure sensors using conductive textiles and piezo-resistive films, demonstrating satisfactory repeatability in terms of measurement in the range of 5–10%, which is higher than that obtained with our sensor (3.4%).[47] The reproducibility error of our sensors (20.7%) is in their reported range of 9–32%. Bahadır integrated FSRs into e-textile structures, creating a mathematical model to characterize the relationship between applied force and measured voltage.[21] These studies highlight the potential of textile-based sensors for wearable applications, with improvements in linearity, sensitivity, and repeatability achieved through the careful selection of materials and structures. However, specific performance metrics varied across studies, indicating the need for further optimization in sensor design and fabrication.

The hysteresis response of the reported FSR sensor design in Fig. 4 exhibits a hysteresis error of 6.11%, in an acceptable range suitable for tactile-based resistive pressure sensors already described in the literature. There is an overlap between the curves of compressive and decompressive loading with this plot, such that the curve of decompression at each loading–unloading cycle exhibits constantly lower resistance levels. There is an asymmetry, indicating a combined effect of the viscoelastic relaxation of the textile substrate and the structural rearrangement of conductive yarn contacts, which together contribute to the observed hysteresis. Our recorded hysteresis compares well with existing research. Tangsirinaruenart and Stylios, for instance, recorded a hysteresis of 6.25% in the embroidered strain gauges that they developed, whereas Goy *et al.* recorded hysteresis levels between 5 and 10% in textile-based pressure sensors with piezoresistive coatings.[45,47] In a similar work, Bahadır reported hysteresis effect ranges between 7% and more than 12% depending on the level of layering in textiles as well as sensor geometrics.[21] In comparison with such baselines, our sensor displays a low degree of hysteresis error (6.11%), showing good mechanical durability and stabilization of emitted signals in repeated loading, which is of particular relevance in dynamic contexts such as gait studies. These findings indicate the potential successful performance of embroidery-based FSR design with regards to hysteresis stability, contemplating its ease of fabrication and complete integration with textiles. The uniform gap between compression and decompression curves throughout cycles further signifies expected behavior as can be compensated algorithmically in upcoming systems of detecting gait phases in real-time applications.

On the basis of the promising performance of the developed and integrated textile-based FSRs, future research and activities will focus on advancing the system toward further applications in gait analysis and rehabilitation. The next phase involves extended testing under dynamic, real-life conditions in healthy volunteers and on the fabricated models that will serve to fine-tune sensor placement, validate calibration models, and assess long-term stability for daily application. At the same time, preparations for human studies will follow established biomedical protocols, including risk assessment, material biocompatibility verification, and system-level safety evaluations that completely correspond to relevant standards and protocols (ISO 13485, IEC 60601). Ethical approvals will be sought for pilot usability studies, which will open the possibility for subsequent clinical trials in patient populations. These steps will ensure system transitions from a laboratory prototype to a robust, user-friendly solution for continuous gait monitoring and rehabilitation support in healthcare settings.[48,49]

5. Conclusions

In this paper, we presented the design, optimization, and characterization of a textile-based FSR for integration into smart socks. After design selection, the FSR used showed a high linear sensitivity of 0.71 Ω/N, as well as a high logarithmic sensitivity of 8.8. Moreover, the hysteresis of the measured sensors showed good overlap in the compression and decompression stages while applying force. The response time of less than 20 ms and the settling force of 111 N of the sensors show promising applicability in future gait analysis devices. Finally, the proposed model for the calibration curve shows a high fit (R^2 score of 99.89%) and low MAE and RMSE values,

making it easy to be integrated into a microcontroller. The literature analysis for optimal FSR placement on the sole of the foot mapped the track for the future research direction.

Acknowledgments

We would like to thank the European Union's Horizon Europe Research and Innovation Programme for providing funding under grant agreement No. 101086348 (Intelligent Wearable System for Enhanced Personalized Gait Rehabilitation - GaitREHub).

References

1 A. Cieza, K. Causey, K. Kamenov, S. W. Hanson, S. Chatterji, and T. Vos: Lancet **396** (2020) 2006. https://doi.org/10.1016/S0140-6736(20)32340-0
2 A. H. M. Ataullah and O. De Jesus: StatPearls (Internet) (StatPearls Publishing, Treasure Island, FL, 2025). https://www.ncbi.nlm.nih.gov/books/NBK560610/
3 N. Voet, V. Altmann, and C. Saris: Neuromuscul. Disord. **33** (2023) S171. https://doi.org/10.1016/j.nmd.2023.07.413
4 Z. Lan, J. Zeng, J. Yan, and K. Chen: Comput. Biol. Med. **171** (2024) 108095. https://doi.org/10.1016/j.compbiomed.2024.108095
5 M. Rezapour, M. R. Mohebbian, and H. Marvi: Bioengineering **12** (2025) 67. https://doi.org/10.3390/bioengineering12010067
6 R. Kumar, P. Bogia, V. Singh, and T. O. Reddy: J. Orthop. **62** (2024) 75. https://doi.org/10.1016/j.jor.2024.10.013
7 World Health Organization: Falls (2025) https://www.who.int/news-room/fact-sheets/detail/falls (accessed July 2025).
8 R. Hayek, S. Aris, G. Al-Refai, and M. Al-Mulla: Sensors **25** (2025) 2310. https://doi.org/10.3390/s25072310
9 D. S. Y. Vun, R. Bowers, and A. McGarry: Gait Posture **112** (2024) 95. https://doi.org/10.1016/j.gaitpost.2024.04.029
10 F. Dierick, M. Penta, P. Renlimiens, and J. L. Thonnard: Gait Posture **20** (2004) 299. https://doi.org/10.1016/j.gaitpost.2003.11.001
11 L. Tesio and V. Rota: Am. J. Phys. Med. Rehabil. **87** (2008) 515. https://doi.org/10.1097/PHM.0b013e31816f17e1
12 Md. Akhtaruzzaman, A. A. Shafie, and Md. R. Khan: J. Mech. Med. Biol. **16** (2016) 1630003. https://doi.org/10.1142/S0219519416300039
13 S. R. Simon: J. Biomech. **37** (2004) 1869. https://doi.org/10.1016/j.jbiomech.2004.02.047
14 Physio-Pedia: The Gait Cycle https://www.physio-pedia.com/The_Gait_Cycle (accessed July 17, 2025).
15 Georgia Southern University: Health and Kinesiology Publications https://digitalcommons.georgiasouthern.edu/health-kinesiology-facpubs/15/ (accessed July 17, 2025).
16 Royal Society: Interface https://royalsocietypublishing.org/doi/10.1098/rsif.2023.0052 (accessed July 17, 2025).
17 PMC: Article PMC10300506 https://pmc.ncbi.nlm.nih.gov/articles/PMC10300506/ (accessed July 17, 2025).
18 bioRxiv: Preprint on Gait Study https://www.biorxiv.org/content/10.1101/2023.01.27.525870v1.full.pdf (accessed July 17, 2025).
19 POPLINE: Document node 385033 https://popline.org/node/385033 (accessed July 17, 2025).
20 G. Laita, A. Buffoli, P. Robert, and G. Langfelder: IEEE Sens. J. **24** (2024) 34162. https://doi.org/10.1109/JSEN.2024.3462598
21 S. K. Bahadır: IEEE Sens. J. **18** (2018) 9770. https://doi.org/10.1109/JSEN.2018.2871396
22 J. Lee, D. Kim, H.-Y. Ryoo, and B.-S. Shin: Sustainability **8** (2016) 466. https://doi.org/10.3390/su8050466
23 C. Erkılıç and A. Yalçın: Gazi J. Econ. Bus. **6** (2020) 006. https://doi.org/10.30855/gjeb.2020.6.3.006
24 V. Morabito: The Future of Digital Business Innovation (Springer, Cham, 2016) Chap. 2. https://doi.org/10.1007/978-3-319-26874-3_2
25 F. M. Sun, C. Zhang, G. Beltrame, and J. Li: Inf. Fusion **53** (2020) 134. https://doi.org/10.1016/j.inffus.2019.06.023
26 A. Salarian, H. Russmann, F. J. G. Vingerhoets, C. Dehollain, Y. Blanc, P. R. Burkhard, and K. Aminian: IEEE Trans. Biomed. Eng. **51** (2004) 1434. https://doi.org/10.1109/TBME.2004.827933
27 F. Lin, A. Wang, Y. Zhuang, M. R. Tomita, and W. Xu: IEEE Trans. Ind. Inform. **12** (2016) 2281. https://doi.org/10.1109/TII.2016.2585643

28 K. Bouchrika: Proc. 3rd Int. Conf. Control, Eng. Inf. Technol. (CEIT) 2015 (IEEE, Tlemcen, 2015) 1–6. https://doi.org/10.1109/CEIT.2015.7233053
29 O. Tirosh, S. J. Preece, R. K. Begg, and D. G. Moore: Proc. 7th Int. Conf. Sensing Technol. (ICST) 2013 (IEEE, Wellington, 2013) 618–622. https://doi.org/10.1109/ICSensT.2013.6727727
30 J. Latsch, S. J. Preece, and R. K. Begg: IEEE Sens. J. **24** (2024) 26472. https://doi.org/10.1109/JSEN.2024.3416847
31 G. Leal-Junior, C. Marques, S. J. Preece, and R. K. Begg: IEEE Sens. J. **18** (2018) 7085. https://doi.org/10.1109/JSEN.2018.2852353
32 P. Ding, J. Yang, S. Wu, and L. Wang: Nano Energy **124** (2024) 109490. https://doi.org/10.1016/j.nanoen.2024.109490
33 J. H. Low, P. S. Chee, E. H. Lim, and V. Ganesan: Smart Mater. Struct. **29** (2020) 065003. https://doi.org/10.1088/1361-665X/ab802c
34 C. Wang, Y. Kim, H. Shin, and S. D. Min: Sensors **19** (2019) 3950. https://doi.org/10.3390/s19183950
35 M. Milovic, R. C. V. Sabino, E. M. J. de Korte, and J. van Luenen: Sensors **22** (2022) 2825. https://doi.org/10.3390/s22082825
36 A. A. Simegnaw, J. Malengier, S. Rotich, B. Malengier, and L. Van Langenhove: Materials **14** (2021) 5113. https://doi.org/10.3390/ma14175113
37 Y. Tai and G. Lubineau: Adv. Funct. Mater. **26** (2016) 600078. https://doi.org/10.1002/adfm.201600078
38 S. K. Manna, M. A. H. Bin Azhar, and A. Greace: Heliyon **9** (2023) e15210. https://doi.org/10.1016/j.heliyon.2023.e15210
39 M. F. Shaikh, Z. Salcic, and K. Wang: Proc. 6th Int. Conf. Automation, Robotics and Applications (ICARA) 2015 (IEEE, Queenstown, 2015) 370–375. https://doi.org/10.1109/ICARA.2015.7081176
40 A. Hoseini, S. H. Hosseini-Zahraei, and A. Akbarzadeh: Proc. ICBME 2022 (IEEE, 2022) 333–339. https://doi.org/10.1109/ICBME57741.2022.10052821
41 W. Heng, J. Li, and J. Yan: Sensors **19** (2019) 5197. https://doi.org/10.3390/s19235197
42 U. Pant, S. Baral, A. Gupta, and P. Shrestha: IOP Conf. Ser.: Mater. Sci. Eng. **1314** (2024) 012008. https://doi.org/10.1088/1757-899X/1314/1/012008
43 E. Gutierrez, V. Gómez, L. Paredes-Madrid, and H. Colorado: Sens. Bio-Sens. Res. **26** (2019) 100300. https://doi.org/10.1016/j.sbsr.2019.100300
44 L. Paredes-Madrid, L. Emmi, E. Garcia, and P. G. de Santos: Sensors **11** (2011) 8836. https://doi.org/10.3390/s110908836
45 O. Tangsirinaruenart and G. Stylios: Materials **12** (2019) 1469. https://doi.org/10.3390/ma12091469
46 A. Liang, R. Stewart, and N. Bryan-Kinns: Sensors **19** (2019) 3618. https://doi.org/10.3390/s19163618
47 C. B. Goy, C. M. Valdes, and M. C. Pichel: J. Med. Eng. Technol. **39** (2015) 208. https://doi.org/10.3109/03091902.2015.1022665
48 ISO: ISO 13485:2016, https://www.iso.org/standard/59752.html (accessed July 20, 2025).
49 IEC: IEC 60601-1 Standard, https://webstore.iec.ch/en/publication/2606 (accessed July 20, 2025).